

# Viscous stability properties of a Lamb–Oseen vortex in a stratified fluid

XAVIER RIEDINGER†, STÉPHANE LE DIZÈS  
AND PATRICE MEUNIER

Institut de Recherche sur les Phénomènes Hors Équilibre, CNRS/Universités Aix-Marseille I&II,  
49, rue F. Joliot-Curie, BP 146, F-13384 Marseille cedex 13, France

(Received 6 March 2009; revised 7 October 2009; accepted 8 October 2009)

In this work, we analyse the linear stability of a frozen Lamb–Oseen vortex in a fluid linearly stratified along the vortex axis. The temporal stability properties of three-dimensional normal modes are obtained under the Boussinesq approximation with a Chebychev collocation spectral code for large ranges of Froude numbers and Reynolds numbers (the Schmidt number being fixed to 700). A specific integration technique in the complex plane is used in order to apply the condition of radiation at infinity. For large Reynolds numbers and small Froude numbers, we show that the vortex is unstable with respect to all non-axisymmetrical waves. The most unstable mode is however always a helical radiative mode ( $m = 1$ ) which resembles either a displacement mode or a ring mode. The displacement mode is found to be unstable for all Reynolds numbers and for moderate Froude numbers ( $F \sim 1$ ). The radiative ring mode is by contrast unstable only for large Reynolds numbers above  $10^4$  and is the most unstable mode for large Froude numbers ( $F > 2$ ). The destabilization of this mode for large Froude numbers is shown to be associated with a resonance mechanism which is analysed in detail. Analyses of the scaling and of the spatial structure of the different unstable modes are also provided.

---

## 1. Introduction

Vortices such as the Lamb–Oseen vortex are often considered as robust coherent structures in homogeneous fluids. The goal of the current work is to demonstrate that when such a vortex is placed in a stratified environment it becomes unstable.

Despite the number of works in the literature, the linear stability of a Lamb–Oseen vortex in a homogeneous medium has been demonstrated only recently (Fabre, Sipp & Jacquin 2006). Such a vortex, which has a Gaussian vorticity profile, is considered as more realistic than other discontinuous vortex models such as the Rankine vortex, which have often been used in the literature. As shown by Fabre *et al.* (2006), the linear normal-mode perturbations of the Lamb–Oseen vortex exhibit special properties owing to the continuous vorticity profile. In particular, many inviscid waves, termed Kelvin modes, become damped because of the appearance of a critical-point singularity (Briggs, Daugherty & Levy 1970; Le Dizès 2000, 2004; Schecter *et al.* 2000; Le Dizès & Lacaze 2005). In a homogeneous fluid, the Lamb–Oseen vortex is stable, and other effects such as axial flow (Lessen & Paillet 1974; Fabre &

† Email address for correspondence: xavier.riedinger@gmail.com

Jacquín 2004), strain field (Eloy & Le Dizès 1999) or other vortices (Le Dizès & Laporte 2002; Meunier & Leweke 2005) have to be added in order to destabilize it.

The effect of stratification has mainly been considered in the context of oceanography and atmospheric sciences under simplifying hypotheses. The first works have been performed in the context of shallow-water flows (see for instance Satomura 1981; Hayashi & Young 1987; Knessl & Keller 1992). For vortices, the destabilizing role of stratification was first demonstrated by Ford (1994). More recently, Schecter & Montgomery (2004) have analysed the stability of a family of Rankine-like vortices under a hydrostatic hypothesis and have obtained a formal expression for the instability growth rate. They have also shown, using wave activity concepts, that the instability is associated with internal gravity wave emission. Further studies have also been performed in a more applied context (Schecter & Montgomery 2006; Hodyss & Nolan 2008; Schecter 2008). The stability of a strongly stratified Rankine vortex has also been considered in Billant & Le Dizès (2009). Asymptotic expressions in the small-Froude-number limit have been derived.

The analysis of stratified Lamb–Oseen vortex started with the works of Miyazaki & Fukumoto (1991) and Le Dizès (2008), who demonstrated the existence of neutral radiative inviscid modes. The instability has been demonstrated only recently in Le Dizès & Billant (2009; see also Le Dizès & Billant 2006). By using a large-wavenumber asymptotic approach (Billant & Gallaire 2005; Le Dizès & Lacaze 2005), Le Dizès & Billant (2009) have shown how the emission of internal gravity waves can become destabilizing in certain conditions and have moreover obtained explicit formulae for the inviscid growth rate that compare very well to numerical results for small Froude numbers. In the present work, this theory will also be used to explain some of the characteristics of the instability for large Reynolds numbers. Interestingly, we shall demonstrate that the Lamb–Oseen vortex is also unstable for small Reynolds numbers and for large Froude numbers.

The effect of stratification on Taylor–Couette flows has been investigated for many years. It was first thought that stratification stabilizes the centrifugal instability (Withjack & Chen 1974, 1975; Boubnov, Gledzer & Hopfinger 1995). But it was recently found that stratification can also have a destabilizing effect in certain regions of the parameter space (Molemaker, McWilliams & Yavneh 2001; Yavneh, McWilliams & Molemaker 2001; Le Bars & Le Gal 2007). This so-called strato-rotational instability (SRI) is associated with a resonance of boundary modes. Such a resonance mechanism has been obtained in several other contexts. Satomura (1981), Hayashi & Young (1987) and Balmforth (1999) have demonstrated its occurrence in shallow-water shear flows. Sakai (1989) and more recently Gula, Plougonven & Zeitlin (2009) have analysed the different types of resonance for a two-layer channel model. Interestingly, we shall demonstrate that in large-Froude-number regime, the Lamb–Oseen vortex is also unstable because of a resonance of Kelvin and radiative modes.

The works on acoustic modes in jets (Luo & Sandham 1997) and in vortices (Broadbent & Moore 1979) and on accretion disks (Papaloizou & Pringle 1984; Narayan, Goldreich & Goodman 1987) where the instability is also due to either wave emission or wave resonance are also worth mentioning.

Finally, one has to note that the instability we shall consider here is different from the so-called zigzag instability which occurs for vortex pairs in a strongly stratified fluid (Billant & Chomaz 2000; Otheguy, Chomaz & Billant 2006).

The paper is organized as follows. In §2, the base flow and the linear stability equations are given. We also discuss the radiative boundary conditions to apply

to the perturbations. We show that these boundary conditions can be implemented with a spectral code to weakly damped modes by performing the integration in the complex plane. The spectral collocation code is briefly presented in this section. In §3, the stability results are presented for the most unstable modes which correspond to helical modes ( $m = 1$ ). Two types of modes are shown to become the most unstable. Stability diagrams (growth rate contours) are obtained for each mode as functions of the Reynolds and Froude numbers. The structure of the eigenmodes is provided, and the role of the critical points in the damping of the modes is also discussed. An important subsection is concerned with the mechanism of resonance which explains the instability for large Froude numbers. A criterion for its occurrence is in particular provided. Results for higher azimuthal wavenumbers  $m \geq 2$  are presented in §4. The last section provides a summary of the main results.

## 2. Framework and numerical method

### 2.1. Base flow and perturbation equations

We consider an axisymmetrical Lamb–Oseen vortex in a viscous fluid of kinematic viscosity  $\nu$ , stably stratified along the vortex axis. The stratification is assumed to be linear with a constant Brunt–Väisälä frequency  $N = \sqrt{-g\partial_z\rho/\rho_0}$  and a mass diffusivity  $D$ . The vortex is characterized by its radius  $a$  and circulation  $\Gamma$ . It satisfies the Navier–Stokes equations under the Boussinesq approximation (Boulanger, Meunier & Le Dizès 2007) provided that the radius  $a$  increases in time according to  $a = \sqrt{a_0^2 + 4\nu t}$ . In this study, this weak diffusion is neglected such that the vortex is assumed ‘frozen’ with a constant radius  $a$ .

Using  $a$  and  $2\pi a^2/\Gamma$  as characteristic spatial and temporal scales respectively, the angular velocity profile of the vortex can be written as

$$\Omega(r) = \frac{1}{r^2} \left(1 - e^{-r^2}\right). \quad (2.1)$$

Under the Boussinesq approximation, the base flow is then defined by the three parameters, namely the Reynolds number  $Re$ , the Froude number  $F$  and the Schmidt number  $Sc$ , given by

$$Re = \frac{\Gamma}{2\pi\nu}, \quad (2.2a)$$

$$F = \frac{\Gamma}{2\pi Na^2}, \quad (2.2b)$$

$$Sc = \frac{\nu}{D}. \quad (2.2c)$$

Whereas the Froude number and the Reynolds number will be varied in a large range of values, the Schmidt number will be fixed to 700, a value commonly used for salted water.

Infinitesimal disturbances of the velocity, pressure and density fields are considered in the form of normal modes,

$$(u', v', w', p', \rho') = [u(r), v(r), w(r), p(r), \rho(r)] \exp(ikz + im\theta - i\omega t), \quad (2.3)$$

where  $u'$ ,  $v'$  and  $w'$  are the radial, azimuthal and axial velocities;  $r$  is the radial coordinate;  $k$  and  $m$  are the axial and azimuthal wavenumbers; and  $\omega$  is the complex frequency. The normal-mode amplitudes satisfy the following equations obtained by

linearizing the Navier–Stokes equations under the Boussinesq approximation:

$$i\Phi u - 2\Omega v = -\frac{dp}{dr} + \frac{1}{Re} \left( \Delta u - \frac{u}{r^2} - \frac{2im}{r^2} v \right), \quad (2.4a)$$

$$i\Phi v + \left( 2\Omega + r \frac{d\Omega}{dr} \right) u = -\frac{imp}{r} + \frac{1}{Re} \left( \Delta v - \frac{v}{r^2} + \frac{2im}{r^2} u \right), \quad (2.4b)$$

$$i\Phi w = -ikp - \frac{1}{F^2} \rho + \frac{1}{Re} \Delta w, \quad (2.4c)$$

$$i\Phi \rho = w + \frac{1}{ReSc} \Delta \rho, \quad (2.4d)$$

$$\frac{1}{r} \frac{d(ru)}{dr} + \frac{imv}{r} + ikw = 0, \quad (2.4e)$$

where  $\Delta = (\partial^2/\partial r^2) + (1/r)(\partial/\partial r) - k^2 - (m^2/r^2)$  is the Laplacian operator written in cylindrical coordinates and

$$\Phi = -\omega + m\Omega. \quad (2.5)$$

This system can be further reduced by eliminating pressure and axial velocity to obtain a third-order system of the form  $\omega A \mathbf{f} = B \mathbf{f}$  for  $\mathbf{f} = [u(r), v(r), \rho(r)]$ . This reduced system together with adequate boundary conditions at the origin and at infinity defines a generalized eigenvalue problem for the frequency  $\omega$ , for fixed base-flow parameters  $(Re, F, Sc)$  and fixed real axial wavenumber  $k$  and azimuthal wavenumber  $m$ . The two symmetries of the equations  $(m, \omega, k, u, v, w, \rho, p) \rightarrow (m, \omega, -k, u, v, -w, -\rho, p)$  and  $(m, \omega, k, u, v, w, \rho, p) \rightarrow (-m, -\bar{\omega}, k, \bar{u}, \bar{v}, -\bar{w}, -\bar{\rho}, \bar{p})$  allow us to limit the study to positive axial wavenumber  $k$  and positive azimuthal wavenumber  $m$ . Standing waves are obtained as combinations of  $m$  and  $-m$ ,  $k$  and  $-k$  modes. Our goal is to determine the unstable eigenmodes which are those with a positive growth rate  $\text{Im} \omega$ , when all the parameters (except  $Sc$ ) are varied. Because we want to provide the marginal curves of the unstable modes, we will also consider neutral and weakly damped eigenfrequencies.

## 2.2. Boundary conditions and numerical method

The boundary conditions that we shall apply to the perturbations are prescribed by causality. Because the fluid is at rest at infinity, we should be able to form the perturbations from a compact initial condition. This condition implies that when the medium can sustain waves at infinity, these waves must propagate outward. The condition of causality is thus in this case a condition of radiation. The difficulty with this condition is that it does not necessarily imply that the solution vanishes at infinity when the modes are neutral or damped ( $\text{Im} \omega < 0$ ).

In order to express the condition of radiation, it is necessary to determine the possible behaviours of the perturbations at  $\infty$ . These can be easily derived by manipulating (2.4a–e) in the large- $r$  limit. We obtain eight independent solutions with an asymptotic behaviour of the form  $r^{\alpha_j} e^{\pm i\beta_j r}$ , where the radial wavenumbers  $\beta_j$  satisfy the equation

$$\left[ \left( \frac{(\beta^2 + k^2)^2}{Re^2 Sc} - i\omega \frac{(\beta^2 + k^2)}{Re} \left( 1 + \frac{1}{Sc} \right) - \omega^2 \right) (\beta^2 + k^2) + \frac{\beta^2}{F^2} \right] \left( \frac{(\beta^2 + k^2)}{Re} - i\omega \right) = 0. \quad (2.6)$$

Two of the solutions of this equation, say  $\pm\beta_1$ , can be considered as ‘non-viscous’ and are such that  $\beta_1 = k\omega/\sqrt{F^{-2} - \omega^2} + O(1/\sqrt{Re})$ . The other six are associated

with diffusion processes and depend on the Reynolds number at leading order. The condition of radiation means that the perturbations should be only composed of waves propagating outward at infinity. The property of these waves is that they are spatially damped as  $r$  increased when they correspond to a positive growth rate  $\text{Im } \omega > 0$ . The condition of radiation thus imposes that the solutions should behave near  $\infty$  as

$$f \sim \sum_{j=1}^4 f_j r^{\alpha_j} e^{i\beta_j r}, \quad (2.7)$$

where the radial wavenumbers  $\beta_j$  have been chosen such that  $\text{Im } \beta_j > 0$  when  $\text{Im } \omega > 0$ . When  $\text{Im } \omega \leq 0$ ,  $\beta_j$  should be obtained by analytical continuation from their definition for  $\text{Im } \omega > 0$ . When  $\text{Im } \omega > 0$ , the above condition is equivalent to the vanishing of the solution at  $\infty$ . But this is not always the case for  $\text{Im } \omega \leq 0$ . In particular, if one  $\text{Im } \beta_j$  has changed sign, the solution prescribed by the condition of radiation is no longer bounded but increases exponentially as  $r$  goes to infinity. In that case, the condition of radiation means that the inward wave corresponding to the exponentially decreasing behaviour  $r^{\alpha_j} e^{-i\beta_j r}$  as  $r$  goes to  $\infty$  should not be part of the solution near infinity. This is *a priori* a condition difficult to implement numerically with a spectral code. With the spectral code we shall use, the condition we shall implicitly apply is that the solution vanishes at infinity. As a consequence, we would not be able to provide the eigenfrequencies in frequency domains in which the physical condition of radiation is not equivalent to the vanishing of the solution.

To get round this difficulty, we consider the problem on a complex path of the form  $r = se^{i\theta}$ ,  $s \in \text{Re}$  with a small fixed value of  $\theta$ . The boundary conditions are then implemented in the complex plane by assuming that the behaviour prescribed by the condition of radiation is also valid along the complex path as  $s$  goes to  $\infty$ . By doing so, we modify the frequency domain in which the condition of radiation is equivalent to the spectral condition of vanishing and therefore change the frequency domain which can be resolved numerically.

This domain of the complex  $\omega$  plane is delimited by curves which define the so-called continuous spectrum. These curves can be obtained by solving (2.6) with respect to  $\omega$ . They are defined by the parametric expressions

$$\omega = -i \frac{\beta^2 + k^2}{Re}, \quad (2.8a)$$

$$\omega = -i \frac{\beta^2 + k^2}{2Re} \left( 1 + \frac{1}{Sc} \right) \pm \sqrt{-\frac{(\beta^2 + k^2)^2}{4Re^2} \left( 1 - \frac{1}{Sc} \right)^2 + \frac{\beta^2}{F^2(\beta^2 + k^2)}}. \quad (2.8b)$$

When we stay on the real axis, the continuous spectrum is obtained by varying  $\beta$  with  $\text{Im } \beta = 0$ . On a complex path of the form  $r = se^{i\theta}$ ,  $\beta$  should be varied with the condition  $\text{Im } \beta e^{i\theta} = 0$ . In figure 1, we have represented the continuous spectrum for typical parameters for a real path and for a complex path with  $\theta = \pi/10$ . As discussed above, these curves delimit the ‘unphysical’ frequency domain in which the vanishing of the solution at  $\infty$  does not correspond to the condition of radiation. This figure illustrates the interest of using a complex path. We clearly see the deformation of the continuous spectrum and the enlargement of the domain in which the condition of radiation can be correctly prescribed by the spectral code. Note in particular that the frequency domain of interest indicated in grey is far from the unphysical domain only if the integration is performed in the complex plane.

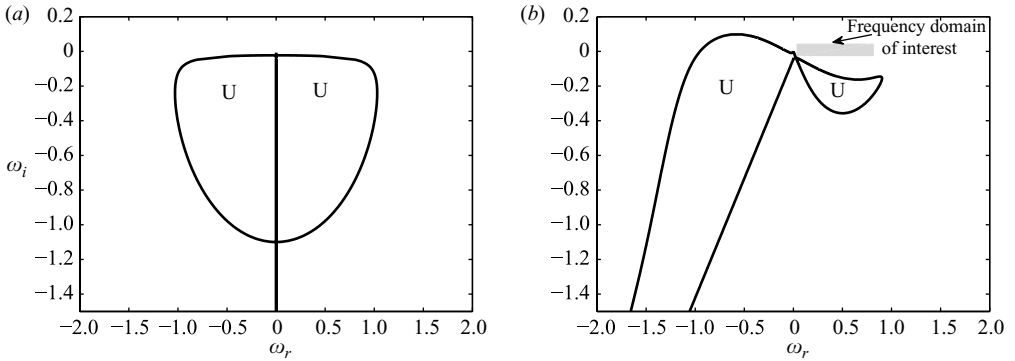


FIGURE 1. Continuous spectrum (solid lines) and ‘unphysical’ domain (indicated by the letter ‘U’) for  $Re=200$ ,  $F=0.9$ ,  $k=3$ . (a) Real path  $\theta=0$ ; (b) complex path  $\theta=\pi/10$ .

It is worth mentioning that this technique could be used in other contexts where unbounded solutions are physically relevant. For instance, Healey (2006) has obtained new convectively unstable modes in the rotating-disk boundary layer, which exhibit exponential growth normal to the disk. We may argue that such modes could probably be obtained with a spectral code by integrating the Rayleigh equation in the complex plane.

On the real axis or on the complex path, the numerical resolution of the eigenvalue problem mainly follows the analysis which was performed by Fabre & Jacquin (2004) for a vortex in a non-stratified fluid. We use a similar Chebychev spectral collocation code, which was, for the present analysis, initially developed by Antkowiak & Brancher with Matlab for non-stratified fluids. As in Fabre & Jacquin (2004), we have used the parity properties of the solutions and have implemented these symmetries on the Chebychev decomposition to speed up the calculation. We have also used a similar mapping from  $s \in [-\infty; \infty]$  to the Chebychev domain  $\xi \in [-1; 1]$  to avoid the treatment of the regular singularity at the origin. With this mapping, the complex radial coordinate is connected to the Chebychev variable by the relation

$$r = (H\xi/(1 - \xi^2))e^{i\theta}. \quad (2.9)$$

We have usually taken values of  $H$  between 1 and 12 and of  $\theta$  between 0 and  $\pi/10$ . Fabre & Jacquin (2004) have shown that the eigenvectors automatically satisfy the boundary conditions at the origin, and we refer to their paper for more details. The number  $Np$  of polynomials was varying between 80 and 500. In practice,  $Np=80$  was often sufficient to describe correctly the modes. Larger values of  $Np$  were mainly used to test the convergence of the eigenvalues.

The numerical spectrum obtained with  $Np=400$  and  $H=12$  for the parameters of figure 1 is shown in figure 2. With these figures, we want to show that the genuine eigenfrequency  $\omega \approx 0.128 - 0.028i$ , indicated by an arrow in figure 2(b), can only be obtained with a complex path. The behaviour of the corresponding eigenmode at infinity is  $e^{\beta_1 r}$  with  $\beta_1 \approx 0.348 - 0.077i$ . With a real path, this frequency is behind the continuous spectrum and is not obtained by the code. It is also interesting to note that for both cases, most of the numerical eigenvalues align very well along with the curves of the theoretical continuous spectrum, and this provides confidence that our numerical eigenvalue computation is correct. There is a discrete eigenvalue near  $\omega \approx 0.1 - 0.05i$ , which is close to the correct eigenfrequency but inside the unphysical domain. This unphysical mode is not linked to the correct eigenvalue at

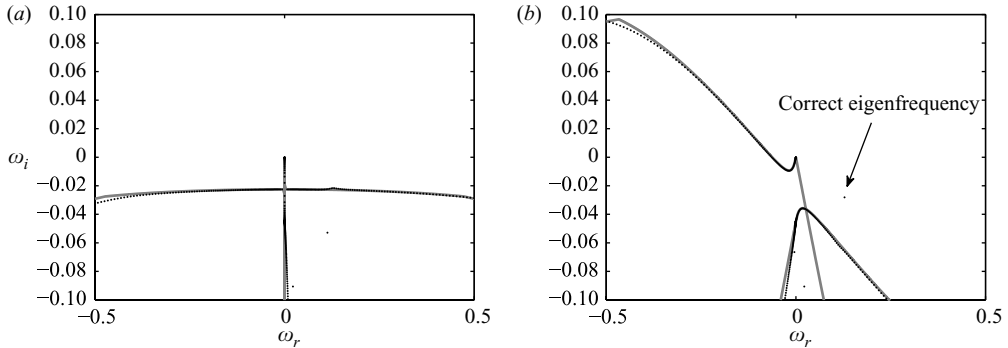


FIGURE 2. Close view of the numerical spectrum (dots) and theoretical continuous spectrum (solid grey lines) near a correct damped eigenvalue (indicated by the arrow) for the parameters of figure 1 and  $Np = 400$  and  $H = 12$ . (a) Real path  $\theta = 0$ ; (b) complex path  $\theta = \pi/10$ .

$\omega \approx 0.128 - 0.028i$ . It disappears, in figure 2(b), as the continuous spectrum sweeps across its location.

Before presenting the results, we would like to mention a second advantage in performing the integration along a complex path. In the inviscid limit, the perturbation equations possess critical-point singularities where  $-\omega + m\Omega(r) = 0$  or  $-\omega + m\Omega(r) = \pm 1/F$ . When  $\omega$  is real, these singularities can be on the real axis. By integrating along the line  $r = se^{i\theta}$  with  $\theta = \pi/10$ , these singularities are thus avoided. Moreover, for the eigenvalues that we will consider, which will satisfy  $0 < \omega_r < m$  for  $m > 0$  (see the grey region in figure 1b), the way they are avoided corresponds to the prescription obtained by causality. The critical points are indeed in the negative imaginary half-plane when  $\text{Im } \omega > 0$ : they should therefore be avoided in the positive imaginary half-plane. In the presence of a small amount of viscosity, the singularities disappear, but viscous scales appear close to the critical points, as well as in large domains of the complex plane (Le Dizès 2004). By integrating in the complex plane, these viscous regions are avoided. The eigenmode structure then remains mainly non-viscous on the integration contour. It can therefore be better resolved with a small number of polynomials. The interest of such an approach has also been demonstrated by Fabre *et al.* (2006).

### 3. Instability of helical modes ( $m = 1$ )

Unstable modes have been obtained for  $m = 1, 2, 3$  but not for  $m = 0$ . The helical modes ( $m = 1$ ) have been found to be the most unstable. They are presented first.

#### 3.1. Unstable-mode characteristics

Results in the inviscid and strongly stratified limits have been obtained and discussed in Le Dizès & Billant (2009). They have used a shooting method to obtain the dispersion relation of the unstable helical modes ( $m = 1$ ). For small Froude numbers, they have shown that the Lamb–Oseen vortex exhibits an infinite number of unstable inviscid modes and that the frequencies of these modes depend only on the product  $kF$ . Their results are compared with the present spectral-code results for a Froude number  $F = 0.9$  in figure 3. Only the first four unstable branches have been plotted. The good agreement with an error smaller than 1% constitutes a validation of the code.

The first mode, which is the most unstable for these parameters, is special, as it is unstable in a finite interval of  $kF$  ( $kF \in [0, 8]$  in figure 3). It also exhibits a special

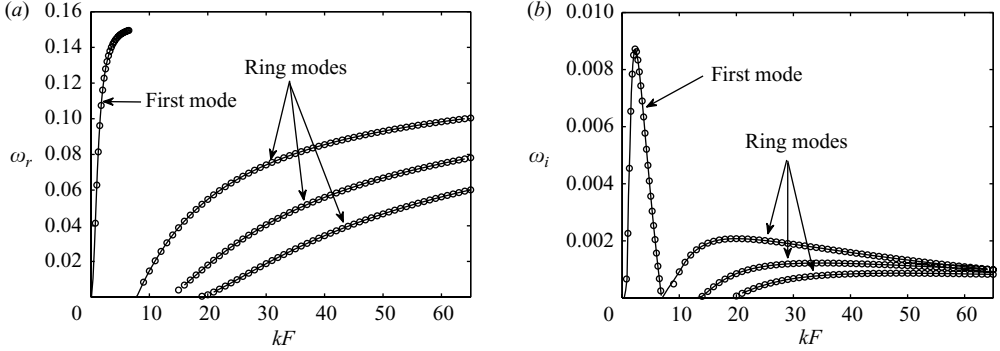


FIGURE 3. (a) Frequency  $\omega_r$  and (b) growth rate  $\omega_i$  of the first four more unstable modes for  $Re = \infty$ ,  $F = 0.9$ . The symbols represent our results with  $Np = 150$ ,  $H = 3$ ,  $\theta = \pi/10$ . The lines represent results obtained by the shooting method of Le Dizès & Billant (2009). Only the unstable modes have been plotted.

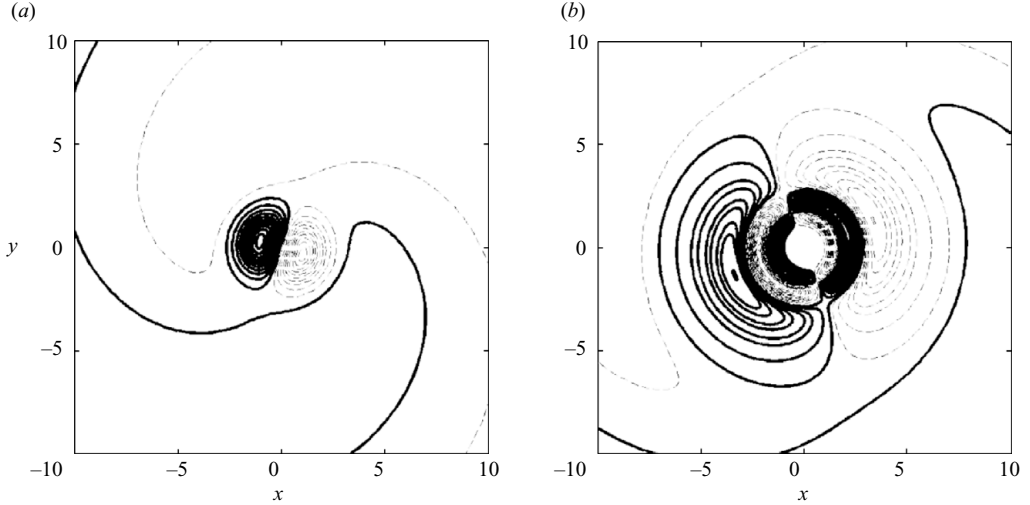


FIGURE 4. Density structure of the first two most unstable helical modes for  $F = 0.9$  and  $Re = \infty$ . (a) First mode obtained for  $k = 2.5$ ,  $\omega = 0.126 + i0.0078$ ; (b) second mode (first ring mode) obtained for  $k = 22.1$ ,  $\omega = 0.055 + i0.00206$ . The solid lines (respectively dashed lines) are the positive (respectively negative) contours.

structure which, compared with the other modes, is mainly localized in the vortex core (see figure 4a). In contrast, all the other modes are unstable in an infinite-wavenumber interval  $[k_n, \infty[$ . As shown in Le Dizès & Billant (2009), the properties of these modes, as well as the instability mechanism, can be understood by using a large-wavenumber Wentzel–Kramers–Brillouin–Jeffreys (WKBJ) analysis. They have demonstrated that all these modes exhibit the same structure. They are mainly localized in a ring region and discretized by the number of half-oscillations in this region. Following the terminology introduced in Le Dizès & Lacaze (2005), we shall call these modes ring modes. All modes including the first mode (non-ring mode) exhibit a radiative part, composed of internal gravity waves, which extends to infinity and which is responsible for the destabilization. The density structure of the second mode, which

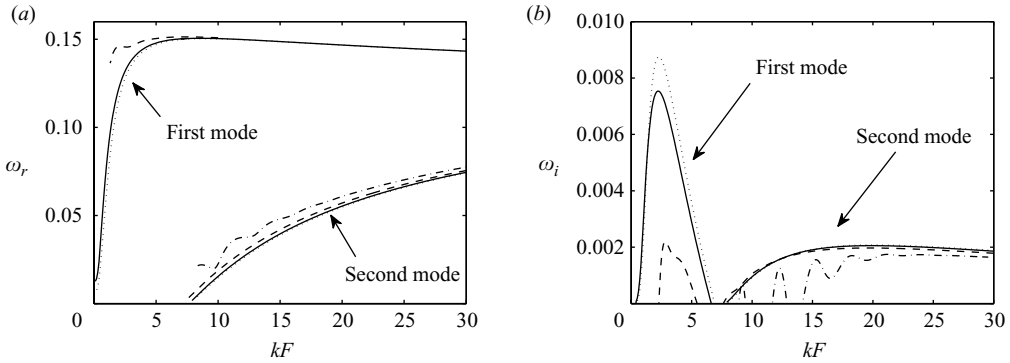


FIGURE 5. Variation of the first two branches with respect to the Froude number in the weakly stratified case for  $m=1$  and  $Re=\infty$ . (a) Frequency  $\omega_r$  and (b) growth rate  $\omega_i$  versus  $k$ , for  $F=0.1$  (dotted line),  $F=1$  (solid line),  $F=2$  (dashed line) and  $F=3$  (dash-dotted line).

corresponds to the first ring mode is plotted in figure 4(b). Both the localization in a ring and the radiative part are visible in this figure. Note also that the amplitude of the ring mode is negligible in the vortex core, in contrast with the first mode shown in figure 4(a). In the geophysical fluid dynamics community, the ring modes correspond to the so-called vortex Rossby waves (Schecter & Montgomery 2004) because they are weakly retrograde waves and are mainly localized in the region in which the (potential) vorticity varies. They differ from the three-dimensional Kelvin modes of vortices in homogeneous fluid (Kelvin 1880), which disappear or become strongly damped for small Froude numbers.

The effects of the viscosity and of the stratification on the first two modes are shown in figures 5 and 7. In figure 5, inviscid characteristics are displayed for various Froude numbers. We clearly see that the frequency and the growth rate are mainly functions of  $kF$  for all  $F$ . For small  $F$ , this property is in agreement with the results of Le Dizès & Billant (2009). Note, however, that for moderate Froude numbers, the growth rate of the modes starts to be affected, especially the first mode. In particular, the growth rate of the first mode strongly decreases as  $F$  increases above 1 and becomes negative when  $F > 2.5$ . The second mode is, by contrast, less damped by an increase of  $F$ . It becomes the dominant mode when  $F > 2$ . For  $F=3$ , we can however note that the growth rate curve changes and exhibits oscillations. As we shall see below, these oscillations are associated with a phenomenon of resonance.

As mentioned above, the eigenmodes possess critical-point singularities where either  $-\omega + m\Omega(r) = 0$  (type I) or  $-\omega + m\Omega(r) = \pm 1/F$  (type II). When the mode becomes neutral some of these singularities are on the real axis. They do not affect the numerical resolution because they remain far from the complex integration contour. For small  $F$ , only type I critical points are present. The role of these critical points was discussed in Schecter & Montgomery (2004) in the limit of vanishing Froude numbers. For large  $F$ , both types of critical points can be present. Here, the critical points which tend to have a stabilizing effect are of type II. These critical points have the same effects as the regular critical points in non-stratified vortices (Le Dizès & Lacaze 2005; Fabre *et al.* 2006). In two dimensions, they are known to damp the modes with a damping rate proportional to the vorticity gradient at the critical point (Briggs *et al.* 1970; Le Dizès 2000; Schecter *et al.* 2000). These modes, which are quasi-modes

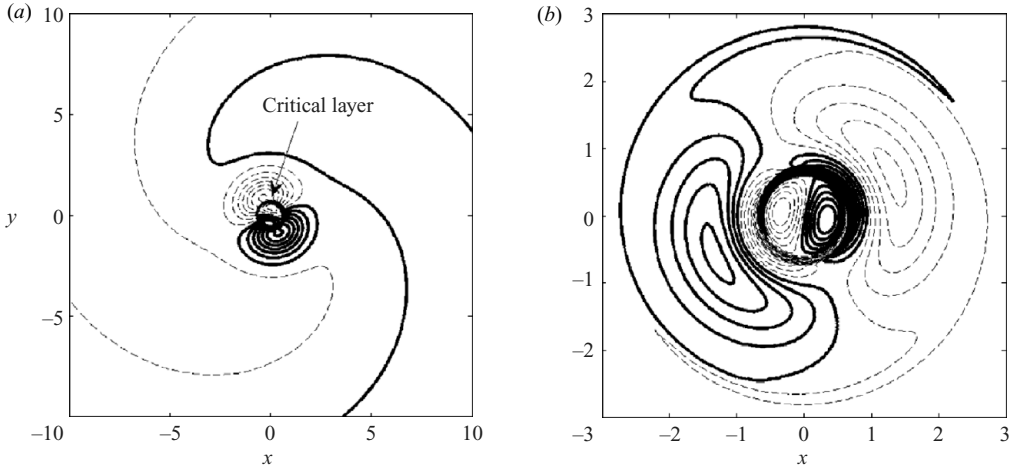


FIGURE 6. (a) Density and (b) vorticity structure of the first helical mode ( $m = 1$ ) for  $F = 1.5$ ,  $Re = 10^5$ ,  $k = 1.6$ ,  $\omega = 0.136 + 0.00538i$ . The critical radius is here  $r_c \approx 0.68$ .

in the inviscid limit, intervene in the rapid axisymmetrization process of perturbed vortices (Schecter *et al.* 2000; Hall, Bassom & Gilbert 2003). In the geophysical context, the critical-layer damping has also been used to interpret the spontaneous alignment of quasi-geostrophic vortices (Schecter, Montgomery & Reasor 2002). In contrast, critical points of type I tend to have a destabilizing role (Le Dizès & Billant 2009).

In the present study, it is the appearance of type II critical points which can explain the progressive stabilization of the eigenmodes when  $F$  is increased above 1. The trace of such a critical point is visible in the eigenmode structure, as illustrated in figure 6. Compare, in particular, figures 6(a) and 4(a) which display the density structure of the first mode respectively with and without the critical layer. Note also the phase change of the vorticity structure across the critical layer (see figure 6b). Such a phase change is typical of viscous critical layers.

A critical point of type II is also present in the second mode when  $F$  exceeds 1, but it has a weaker stabilizing effect. More precisely, its stabilizing effect is delayed to higher values of the Froude number. This difference is associated with the different structure of the second mode which is not localized in the vortex core. Critical point II indeed reaches the region in which the second mode is localized for much larger values of  $F$ . We shall come back to this point in §3.3, where the properties of the second mode will be analysed in more detail.

The effect of the Reynolds number on the first two branches is shown in figure 7. We can first notice that the frequencies are almost unaffected by Reynolds number variations. However, as expected, viscosity is stabilizing; moreover, the larger the wavenumber, the stronger the damping. Note for instance that for  $Re = 3000$ , the second mode is completely stable, and the instability band of the first mode has moved to smaller wavenumbers. Surprisingly, we shall see below that viscosity does not kill the instability and that the first mode remains unstable however small the Reynolds number. This small-Reynolds-number behaviour is reminiscent of the Kelvin–Helmholtz instability which is also active for Reynolds numbers of order 1 (Esch 1957). Note, however, that for small Reynolds numbers, viscous diffusion of

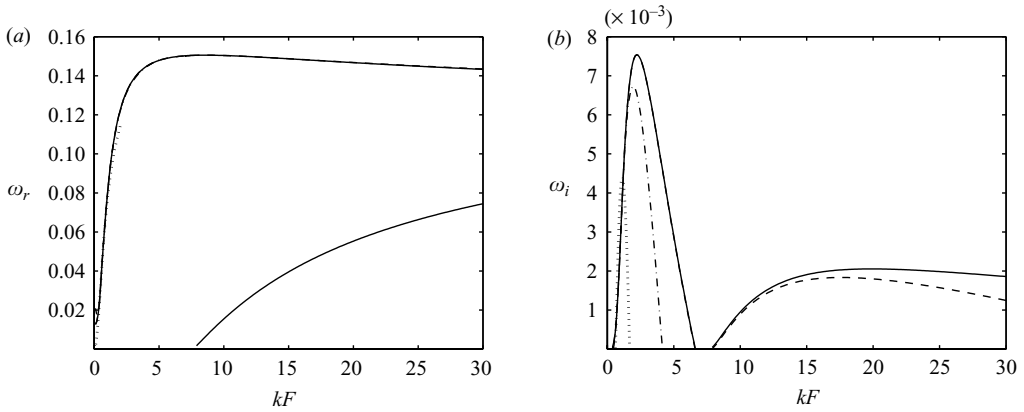


FIGURE 7. Variation of the first two branches with respect to the Reynolds number for  $m = 1$ ,  $F = 1$ . (a) Frequency  $\omega_r$  and (b) growth rate  $\omega_i$  versus  $kF$  for  $Re = \infty$  (solid line),  $Re = 10^6$  (dashed line),  $Re = 3000$  (dash-dotted line),  $Re = 200$  (dotted line).

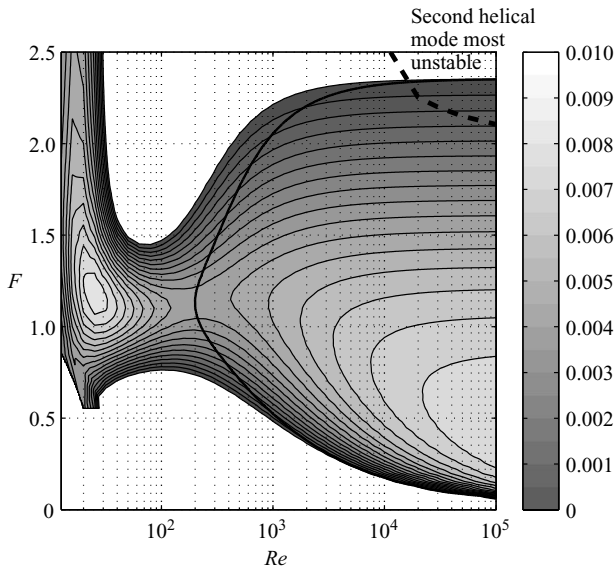


FIGURE 8. Maximum-growth-rate contours (maximum over  $k$ ) of the first helical mode ( $m = 1$ ) as a function of the base-flow parameters  $F$  and  $Re$ . The dashed curve delimits the unstable region in which the first helical mode is not the most unstable mode. The thick solid curve delimits the region in which the growth rate is larger than  $1/Re$ . To the left of this curve, the viscous diffusion of the base flow is expected to affect the results.

the base flow is no longer negligible. The unstable character of the ‘frozen’ base flow for small Reynolds numbers may not be useful in practice.

### 3.2. Instability properties of the first helical mode

We now detail how the properties of the first helical mode vary with  $F$  and  $Re$  when it is the most unstable mode. The maximum-growth-rate contours (maximum over all  $k$ ) of the first helical mode in the  $(Re, F)$  plane are shown in figure 8. We have also indicated in this figure the parameter region in which the first mode is no

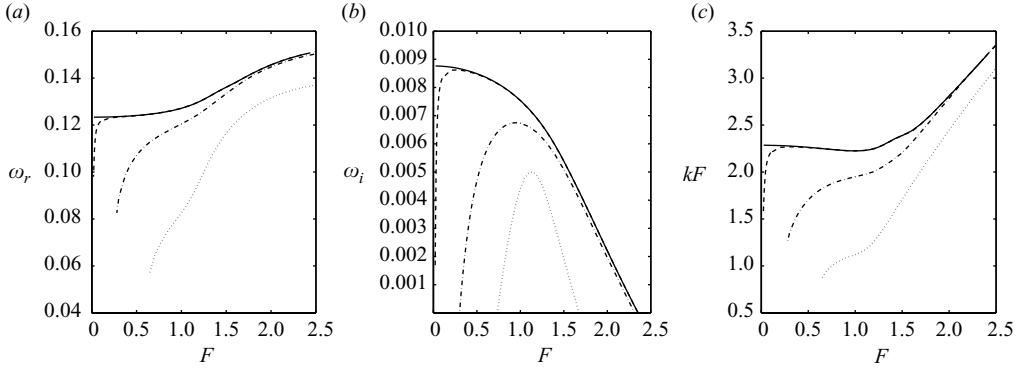


FIGURE 9. Characteristics of the most unstable first helical mode for  $Re = \infty$  (solid line),  $Re = 10^6$  (dashed line),  $Re = 3000$  (dash-dotted line),  $Re = 200$  (dotted line) as a function of the Froude number  $F$ . (a) Frequency  $\omega_r$ ; (b) growth rate  $\omega_i$ ; (c) product  $kF$ .

longer dominant. Maximum-growth-rate curves for fixed Reynolds numbers are also shown in figure 9(b). The corresponding frequency  $\omega_r$  and the product  $kF$  of the most unstable mode are displayed in figure 9(a, c). A first point to note is that for  $Re > 200$ , the frequency of the most unstable mode does not vary much with respect to the Froude number and is always between 0.1 and 0.14. The plots of figure 9(c) confirm the scaling mentioned above: the most unstable mode has a wavenumber  $k_{max}$  which scales as  $k_c^-(Re)/F$  for small Froude numbers and large Reynolds numbers, where  $k_c^-(\infty) \approx 2.3$  (from figure 9c). Note, by contrast, that for large Froude numbers, the most unstable wavenumber is mainly constant.

Figure 9(b) demonstrates that only in the inviscid limit, the mode is most unstable for small Froude numbers. Its maximum growth rate  $\omega_i^{max} \approx 8.75 \times 10^{-3}$  is obtained in the inviscid limit for  $F \rightarrow 0$ . The scaling  $k_{max} \sim k_c^-(Re)/F$  explains the stabilization of the mode for small Froude numbers at a finite Reynolds number. This damping is a viscous effect which becomes more and more important as  $F$  decreases because of the divergence of the most unstable wavenumber for vanishing  $F$ . For arbitrarily large but finite Reynolds numbers, we therefore expect a stabilization for sufficiently small Froude numbers. For instance, for  $Re = 10^6$ , the first helical mode becomes stable at  $F = 0.015$ .

The stabilization for large  $F$  owes to the appearance of a critical point of type II. As explained above, the first mode is more affected by this critical point because it appears when  $F$  is increased above 1 in the region in which this mode is localized. This also explains why the second mode can become more unstable than the first mode for large Froude numbers. The region of the parameters in which the second mode is the most unstable has been indicated in figure 8. More details on this mode are given below.

Figure 8 shows that the first mode is not stabilized by viscosity and remains unstable for small Reynolds numbers in a large domain of Froude numbers. The peak of instability of the Lamb–Oseen vortex is reached ( $Re$  for a small Reynolds number  $Re = 26$ ). The characteristics of the most unstable mode over all the parameters are the following:  $\omega = 0.0198 + 0.00879i$ ,  $k = 0.385$ ,  $Re = 26$  and  $F = 1.15$ . The vorticity structure of this mode is given in figure 10(a). It is different from the most unstable mode obtained for infinite Reynolds number and the same Froude number (see figure 10b). It has a simple dipolar structure and resembles a displacement mode.

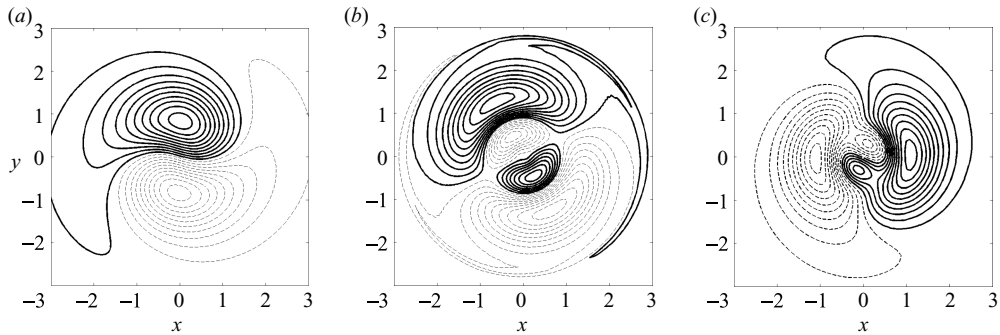


FIGURE 10. Axial vorticity contours in the plane of the first helical eigenmode for  $F = 1.15$  and (a)  $Re = 26$ ,  $k = 0.38$ ,  $\omega = 0.0195 + i0.00878$ , (b)  $Re = \infty$ ,  $k = 1.95$ ,  $\omega = 0.129 + i0.00706$ , (c)  $Re = 80$ ,  $k = 0.8$ ,  $\omega = 0.0682 + i0.00566$ .

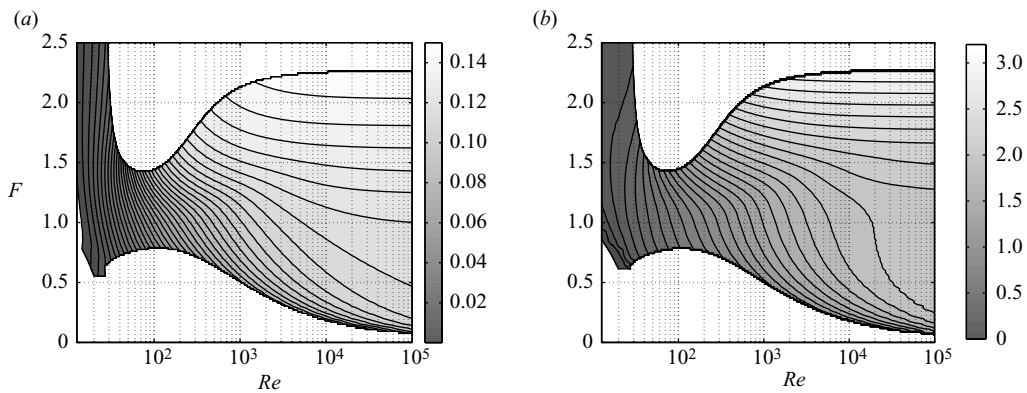


FIGURE 11. Characteristics of the most unstable first helical mode as function of  $F$  and  $Re$ . (a) Isocontours of the frequency  $\omega_r$ ; (b) isocontours of the product  $kF$ .

Interestingly, the structure of the modes changes continuously from figure 10(b) to figure 10(a) as the Reynolds number is decreased. This is illustrated in figure 10(c), where we have plotted the vorticity field of the eigenmode obtained at an intermediate Reynolds number  $Re = 80$ . The continuous variation is also visible in figure 11, where we have displayed the isocontours of the frequency and of the product  $kF$  of the most unstable first mode in the  $(F, Re)$  plane. We clearly see that there is no discontinuity and therefore no jump from one mode to another when either the Reynolds number or the Froude number is varied.

When  $Re$  goes to zero, both the frequency and the wavenumber of the most unstable mode tend to zero as seen in figure 11. Because the numerical method is not adapted to compute very small-wavenumber modes, we have stopped the calculation at  $k = 0.05$ . The left marginal curve obtained in figures 8 and 11 thus corresponds to the marginal curve for a fixed wavenumber  $k = 0.05$ . We suspect that there is no critical Reynolds number if  $k$  is allowed to go to zero.

### 3.3. Instability properties of the second helical mode

As discussed in §3.1, there is an infinite number of unstable helical modes in the inviscid limit. In the previous section, we have given the property of the first mode

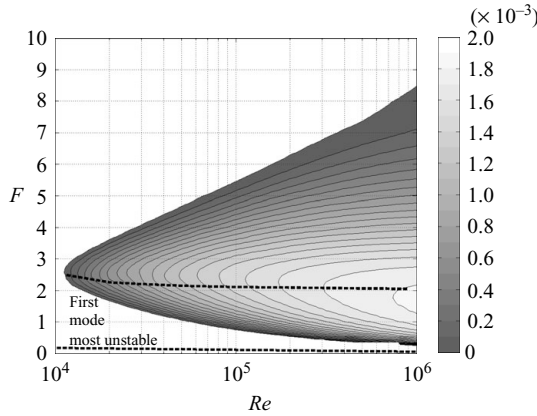


FIGURE 12. Maximum-growth-rate contours of the second helical mode ( $m = 1$ ) as functions of the base-flow parameters  $F$  and  $Re$ . The dashed curves delimit the unstable region in which the first helical mode is more unstable.

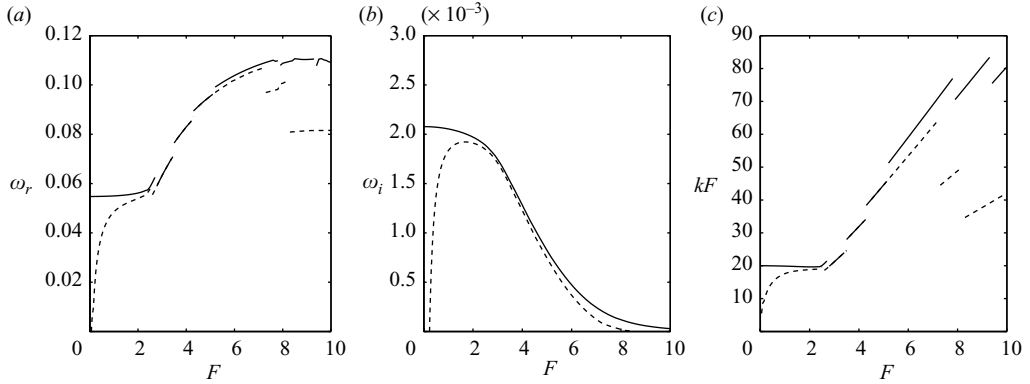


FIGURE 13. Characteristics of the most unstable second helical mode for  $Re = \infty$  (solid line) and  $Re = 10^6$  (dashed line) as a function of the Froude number  $F$ . (a) Frequency  $\omega_r$ ; (b) growth rate  $\omega_i$ ; (c) product  $kF$ .

which is the most unstable mode in a large range of parameters. However, we have also seen that the second mode, which is the first in the family of ring modes, can become more unstable for large Froude numbers. In this section, we provide more information on this mode in this regime.

The maximum-growth-rate contours for this mode as function of the base-flow parameters are shown in figure 12. This plot must be compared with figure 8 which shows the characteristics of the first mode. In contrast with the first mode, the second mode possesses a critical Reynolds number  $Re_c \approx 10^4$  below which it is stable for all Froude numbers. On the other hand, for supercritical Reynolds numbers, the instability domain of the second mode extends to much larger values of the Froude number than the first mode. A large domain of the parameters, which is above the upper dashed line in figure 12, is then dominated by the second helical mode.

As for the first mode, we have represented in figure 13 the frequency and the wavenumber of the most unstable mode for fixed values of the Reynolds number as a function of the Froude number. The first point to note is that the growth rate

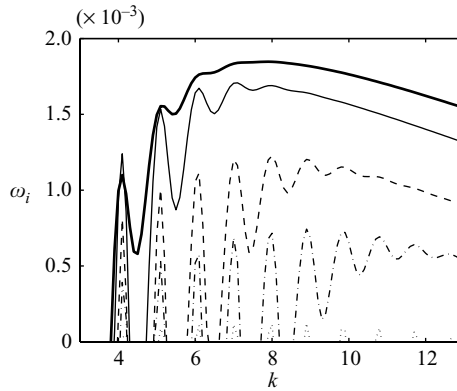


FIGURE 14. Maximum growth rate versus  $k$  of the second helical mode for  $Re = \infty$ :  $F = 2.5$  (thick solid line),  $F = 3$  (solid line),  $F = 4$  (dashed line),  $F = 5$  (dash-dotted line),  $F = 7$  (dotted line).

curves of the second mode shown in figure 13(b), though they extend to larger Froude numbers, are similar to those of the first mode for the same large Reynolds numbers (see figure 9b). The maximum growth rate is also obtained in the inviscid limit as  $F$  goes to 0. It is equal to  $\omega_i^{max} \approx 0.002$ . In this domain of parameters (small Froude, large Reynolds), the second mode is however always less unstable than the first mode.

An interesting aspect of the second mode is seen in figure 13(a, c): the frequency and wavenumber curves exhibit discontinuities as  $F$  varies. No such behaviour was observed for the first mode. These discontinuities are associated with mode jumps. They can be understood by looking at figure 14, where the growth rate of the second mode is plotted versus  $k$  for different Froude numbers. We see in this figure that the growth rate curves exhibit oscillations which become more and more pronounced as  $F$  increases. These oscillations are limited to small values of  $k$ , but they become sufficiently important for large  $F$  to change qualitatively the form of the instability domain. For large  $F$ , the second mode becomes unstable in instability bands centred on fixed wavenumbers which are independent of the Froude number. Each discontinuity observed in the frequency and wavenumber curves in figure 13 corresponds to a change in the most unstable peak.

The origin of these instability peaks can be attributed to a phenomenon of resonance. In figure 15, we have considered a large-Froude-number case in which this phenomenon is clearly visible. We have plotted in figure 15(a) the frequencies of the modes involved in the resonance. The almost vertical dotted lines correspond to damped Kelvin modes. The solid oscillating curve corresponds to the second helical mode. This radiative mode is also damped except when its frequency matches the frequency of one of the Kelvin modes. This is clear evidence of a mechanism of resonance. Note in particular that the axial group velocities  $(\partial\omega_r)/(\partial k)$  of both kinds of modes are opposite. At the crossing point, the energies of the waves are also expected to be opposite in agreement with the condition of instability by resonance (for details, see Cairns 1979; Fukumoto 2003). The Kelvin modes can also be destabilized by a resonance with the third helical mode (which is not plotted in figure 15a because it is too strongly damped). This leads to the bands of instability plotted as the dotted lines in figure 15(b). The fact that the two types of modes simultaneously exist can be understood by using the results of the asymptotic theory performed in Le Dizès &

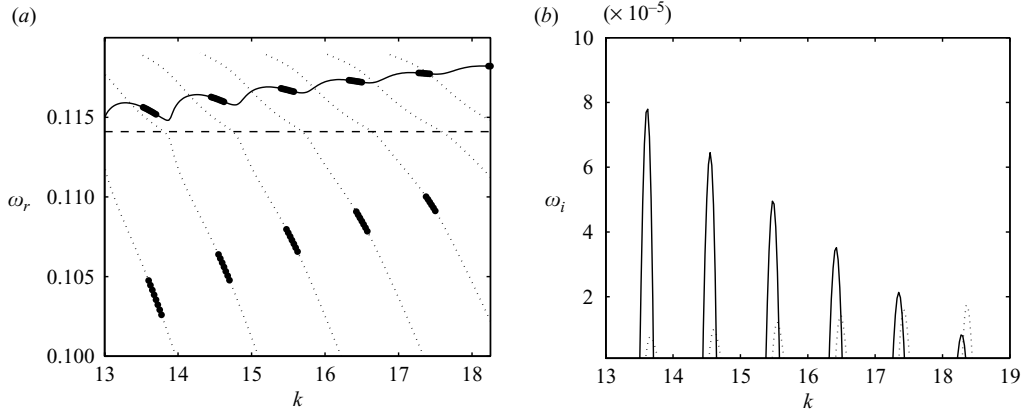


FIGURE 15. Dispersion relation of the helical modes for  $Re = \infty$  and  $F = 8$ . (a) Frequency  $\omega_r$  and (b) growth rate  $\omega_i$ . The modes shown in (a) are damped except in the thick part of the curve where the growth rate is given in (b). The solid and dotted lines correspond to radiative and Kelvin modes respectively. Modes with a growth rate smaller than  $-3 \times 10^{-2}$  have not been plotted in (a). The horizontal dashed line in (a) is the theoretical prediction of maximum resonance.

Lacaze (2005) and Le Dizès & Billant (2009). In Le Dizès & Lacaze (2005), it was shown that for infinite Froude number, inviscid Kelvin modes with frequencies  $0 < \omega_r < 0.13$  do exist. These modes are localized in the vortex core between the centre and a (turning) point  $r_t(\omega_r)$  defined by  $\omega_r = \omega^-(r_t)$  with

$$\omega^-(r) = m\Omega(r) - \sqrt{2\Omega(r)\left(2\Omega + r\frac{d\Omega}{dr}\right)}. \quad (3.1)$$

When stratification is introduced, these Kelvin modes are still present and not immediately affected by the critical point  $r_c$  of type II which appears in their structure. As explained in Le Dizès & Lacaze (2005), the Kelvin modes are expected to remain quasi-neutral as long as this critical point is outside the region in which the mode is localized, that is to say as long as  $r_t(\omega_r) < r_c(\omega_r, F)$ . This is always the case when  $F < 2.59$ . However, when  $F > 2.59$ , this limits the frequency of the quasi-neutral Kelvin modes to an interval  $(0, \omega_l(F))$ , where  $\omega_l(F)$  is defined by  $r_t(\omega_l) = r_c(\omega_l, F)$  (see figure 16). For the radiative modes, we have the opposite problem. As shown by Le Dizès & Billant (2009), these modes are known to be quasi-neutral in the strongly stratified case. In this limit, they possess similar frequencies,  $0 < \omega_r < 0.13$ , as Kelvin modes in the non-stratified case and are localized in the ring region delimited by the two turning points where  $\omega_r = \omega^-(r)$ . The left turning point of this region corresponds to the turning point delimiting the Kelvin mode region. Therefore, both modes are localized in different regions. As for the Kelvin modes, we expect the radiative modes to remain quasi-neutral as long as the critical point does not enter the region in which the mode is localized. When  $F > 2.59$ , this provides a constraint on the allowed frequencies which must satisfy  $\omega_l(F) < \omega_r < 0.13$ . With these large-wavenumber analysis arguments, both types of modes are thus expected to remain quasi-neutral in distinct frequency intervals having the frequency  $\omega_l(F)$  as common boundary (see figure 16). It is therefore around this frequency that we expect a possible mechanism of resonance. This is in agreement with the numerical results obtained for  $F = 8$ . For this value of  $F$ , we have  $\omega_l(8) \approx 0.114$ , which is close to the value for

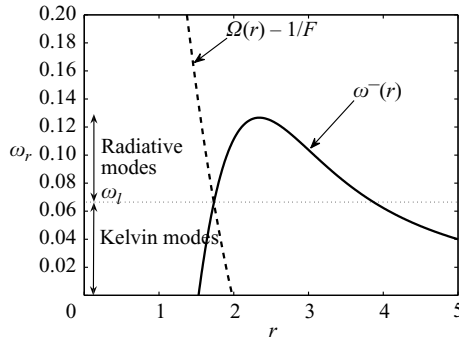


FIGURE 16. Theoretical predictions for the frequency domain of existence of quasi-neutral modes for  $m=1$  and  $F=4$ . The dashed line is the plot of  $\Omega(r) - 1/F$  which defines the location of the critical point II; the solid line is the plot of  $\omega^-(r)$  which defines the location of the turning points.

which the mechanism of resonance is the most efficient (see figure 15). Using these arguments, we predict that the mechanism of resonance is active on the helical ring modes for  $F$  satisfying  $2.59 < F < 18.5$ . Above  $F = 18.5$ , the critical point is within the domain in which the ring modes are localized whatever their frequency. The modes are therefore expected to be too strongly damped to be resonantly excited.

The resonance mechanism is also visible in the structure of the modes. In figure 17(*b–d*), we have plotted the density of the eigenmodes for (*c, d*) two resonant wavenumbers and (*b*) one non-resonant wavenumber for a particular set of parameters. The frequency of these modes has been indicated in figure 17(*a*). In order to plot these modes in the physical space, especially the stable mode (*b*), we have used a particular integration path which is real up to  $r = 20$  and then complex on the line  $r = 20 + se^{i\theta}$  to satisfy the condition of radiation. To facilitate the comparison of the different profiles, we have normalized the density of the eigenmodes such that its maximum amplitude in the radiative domain  $r \in [5; 20]$  is equal to 1. By doing so, we can remark that the amplitude of the mode in the core region  $r < 1.6$  is greater for the unstable cases. The stable mode is by contrast more localized in the critical layer. It is also interesting to compare the number of wavelengths in the core region for the two successive resonant modes shown in figure 17(*c, d*). We can notice that there is one more half-wavelength in figure 17(*d*) than in figure 17(*c*). This is in agreement with the fact that the resonance occurs with two successive Kelvin modes which possess this particular property (Le Dizès & Lacaze 2005).

#### 4. Instability of higher azimuthal wavenumbers: $m = 2, 3, \dots$

For higher azimuthal wavenumbers ( $m \geq 2$ ), unstable modes have also been obtained. Their structure and properties resemble those of the helical ring modes.

In figures 18 and 19, we have plotted the first unstable branches for an inviscid and strongly stratified case for  $m = 2$  and  $m = 3$  respectively. As for the helical ring modes, there are an infinite number of unstable inviscid modes, which are all unstable in semi-infinite-wavenumber intervals. The frequency of each mode increases from zero to a finite value which is 0.4 for  $m = 2$  and 1 for  $m = 3$  as the wavenumber increases. However, the growth rate of each mode reaches its maximum for a finite wavenumber. As for the  $m = 1$  case, we have also observed that for small Froude

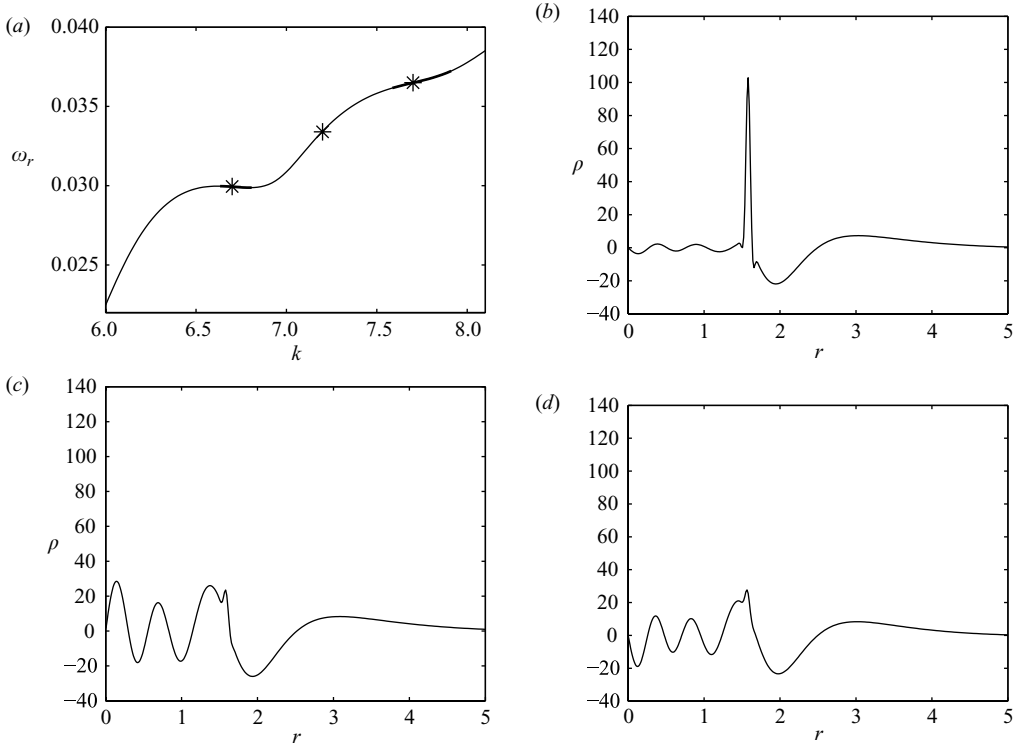


FIGURE 17. Structure of the resonant/non-resonant modes for  $m=1$ ,  $F=3$ ,  $Re=10^5$ . (a) Frequency of the third helical mode (second ring mode). The thick line is the unstable domain. The radial profile of the eigenmode density at the crosses is given in (b)–(d): (b)  $kF=7.2$  (stable); (c)  $kF=6.7$  (unstable); (d)  $kF=7.7$  (unstable).

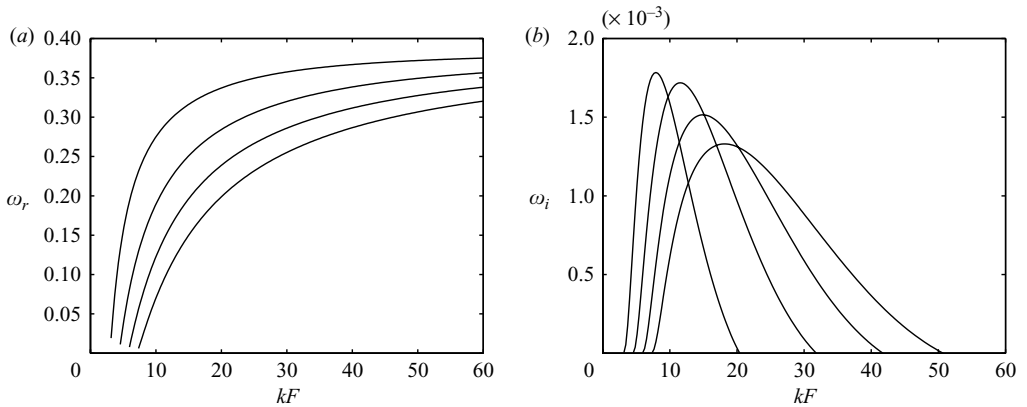
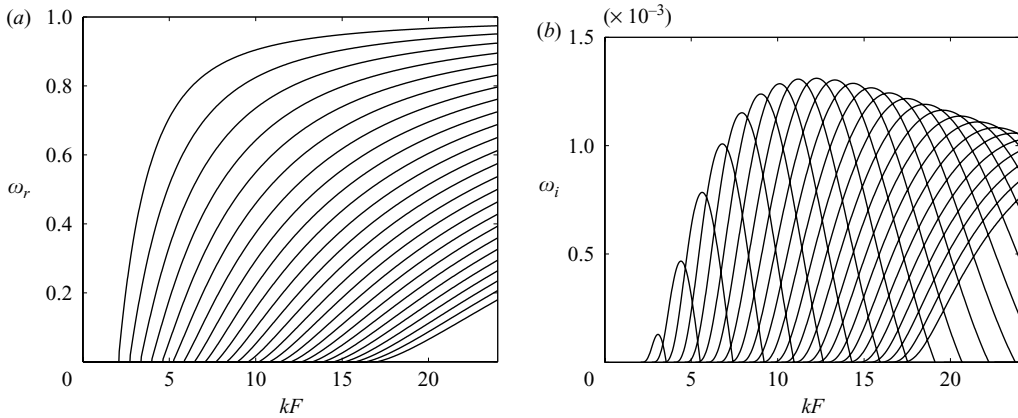
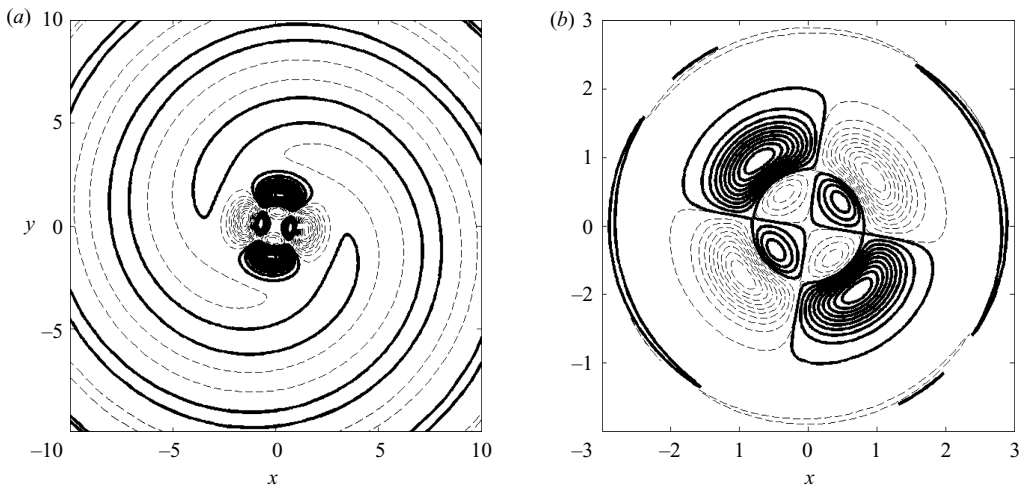


FIGURE 18. (a) Frequency  $\omega_r$  and (b) growth rate  $\omega_i$  for  $m=2$ ,  $Re=\infty$  and  $F=0.3$

numbers, the dependence with respect to the Froude number appears only via a rescaled wavenumber  $kF$ .

The density and vorticity structure of an unstable mode  $m=2$  has been illustrated in figure 20. We can notice in figure 20(a) the radiative zone which extends far


 FIGURE 19. (a) Frequency  $\omega_r$  and (b) growth rate  $\omega_i$  for  $m=3$ ,  $Re = \infty$  and  $F=0.2$ 

 FIGURE 20. Structure of the eigenmode  $m=2$ ,  $k=19.8$  and  $\omega=0.244 + i0.00173$  for  $F=0.4$  and  $Re = \infty$ . (a) Density contours; (b) axial vorticity contours.

from the vortex. In the vorticity plot (figure 20b), we also observe near  $r_c \approx 2.9$  the trace of a critical point of type I. In contrast with the helical modes  $m=1$ , the mode  $m=2$  extends into the core region. This property can be understood from the large-wavenumber asymptotic theory already used above. Using this theory, we expect the eigenmodes to be localized between two turning points corresponding to zeros of the function  $\omega^-(r)$  defined in (3.1). As the left turning point is closer to the centre than for the modes  $m=1$ , the extension of the mode towards the centre is thus more important. For higher azimuthal wavenumbers  $m \geq 3$ , the left turning point disappears, and all the modes become core modes. For  $m=2$ , the two turning points merge for  $\omega \approx 0.4$ . For  $m=3$ , the right turning point collapses to the centre for  $\omega \approx 1$ . We therefore do not expect eigenmodes above these frequencies in agreement with the numerical results shown in figures 18 and 19. With this argument, we can also predict that there exist radiative core modes for all  $m \geq 3$  with frequencies between 0 and  $m-2$ .

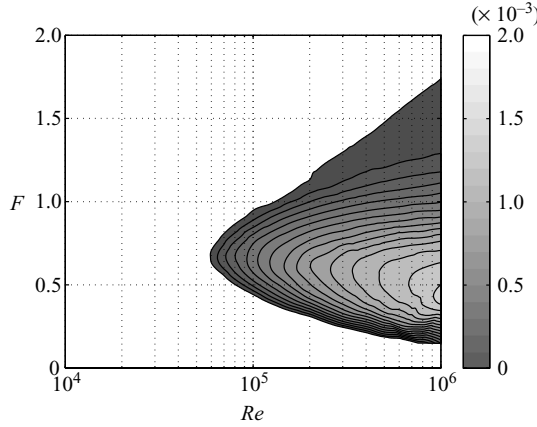


FIGURE 21. Maximum-growth-rate contours of the first mode  $m = 2$  in the  $(Re, F)$  plane.

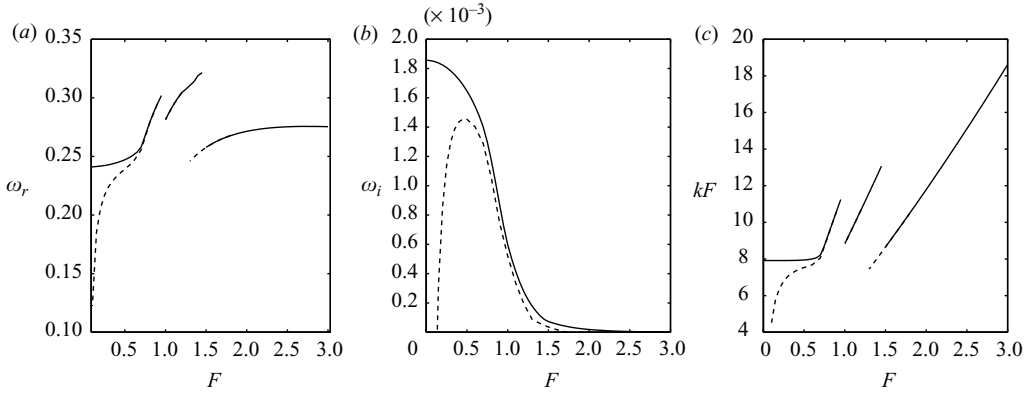


FIGURE 22. Characteristics of the most unstable mode  $m = 2$  as a function of the Froude number for  $Re = \infty$  (solid line),  $Re = 10^6$  (dashed line). (a) Frequency  $\omega_r$ ; (b) growth rate  $\omega_i$ ; (c) product  $kF$ .

For the  $m = 2$  case, the most unstable mode is the first mode (see figure 18). The instability diagram for this azimuthal wavenumber can therefore be obtained by considering the first mode only. In figure 21, we have plotted the maximum-growth-rate contours of this first mode as functions of  $Re$  and  $F$ . If we compare this diagram with the one obtained for the second helical mode (see figure 12), we can notice that the characteristics of the growth rate contours with respect to these parameters are similar. For  $m = 2$ , however, the growth rate values are smaller; the critical Reynolds number is larger; and the maximum growth rate tends to be reached for a Froude number around 0.5 instead of 1 for the modes  $m = 1$ . Yet, in the inviscid limit, the maximum growth rate is also reached for vanishing Froude numbers (see figure 22b). A similar scaling of the most unstable wavenumber with respect to the Froude number is obtained:  $k_{max}$  is constant for large  $F$  but proportional to  $1/F$  for small  $F$ . The mechanism of resonance is also active for the modes  $m = 2$  as can be seen in figure 23. This leads to discontinuities in the plots of the most unstable frequency and wavenumber (see figure 22a, c). However, using the theoretical arguments mentioned

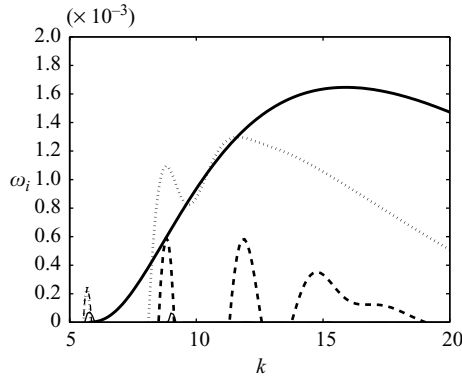


FIGURE 23. Maximum growth rate versus  $k$  of the first mode  $m=2$  for  $Re = \infty$ .  $F=0.5$  (thick solid line),  $F=0.75$  (dotted line),  $F=1$  (dash line),  $F=1.5$  (solid line)

above, we predict that resonance is possible for Froude numbers between 0.5 and 2.8 only.

For  $m=3$  and for larger  $m$ , similar characteristics are obtained, but the modes are less unstable and therefore become destabilized only for larger Reynolds numbers. The large-wavenumber asymptotic theory also predicts that the unstable radiative modes are all core modes and that no phenomenon of resonance is possible at any Froude number.

## 5. Conclusion

In the current work, we have obtained the stability characteristics of a Lamb–Oseen vortex stratified along its axis for a large range of the Froude and Reynolds numbers. We have shown that for moderate Froude number the vortex is unstable at any Reynolds number, with respect to a helical perturbation ( $m=1$ ) which resembles a displacement mode with a radiative structure. For large Reynolds numbers ( $Re > 10^4$ ) and large Froude numbers ( $F > 2$ ), the vortex becomes more unstable with respect to another helical radiative mode which is localized in a ring. Moreover, we have shown that the instability for large Froude numbers is boosted by a mechanism of resonance. We have demonstrated that the radiative mode can enter in resonance with vortex Kelvin modes for particular frequencies in a specific range of Froude numbers. This mechanism selects particular wavenumbers which were found to be independent of the Froude number and which make the vortex unstable up to  $F \approx 10$ . Unstable perturbations with larger azimuthal wavenumbers were also found. All these modes are less unstable than the helical ring mode and exhibit a larger critical Reynolds number. The mechanism of resonance has also been shown to be present for  $m=2$  but not for larger azimuthal wavenumbers.

The results obtained in the present paper could have important consequences for geophysical applications. We have shown that the generic vortex model of the Lamb–Oseen vortex is unstable for large Reynolds numbers in a very large range of Froude numbers. We have also shown that the radiative instability concerns a very large band of wavenumbers. This implies that flat vortices (oceanic vortices, large-scale atmospheric vortices) could still be affected by the instability. In particular we have seen that for  $F > 1$ , helical ring modes are inviscidly unstable for all  $kF$  larger than 8. Note also that in the same Froude number regime, these vortical structures are also

affected by another instability mechanism as soon as they are slightly tilted with respect to the direction of stratification (Boulangier *et al.* 2007; Boulangier, Meunier & Le Dizès 2008).

It is worth mentioning that background rotation has not been considered in the present work. Weak negative background rotation is known to be destabilizing: the vortex becomes unstable with respect to the centrifugal instability. Positive background rotation could by contrast have an opposite effect if inviscid theoretical predictions hold true (Schechter & Montgomery 2004; Le Dizès & Billant 2009). It will therefore be interesting to quantify this stabilizing effect and determine whether it can suppress the present instability.

It is important to emphasize the radiative nature of the unstable modes. We have demonstrated that the geostrophic motion associated with the Lamb–Oseen vortex is able to emit spontaneously internal gravity waves. This phenomenon is a clear illustration that balanced geostrophic motions and unbalanced oscillating motions are strongly coupled and that the evolution of the vortex could not have been predicted by filtering out the unbalanced motions associated with internal gravity waves. Similar interactions between balanced and unbalanced motions have been documented in several recent studies (Molemaker, McWilliams & Yavneh 2005; Williams, Haine & Read 2005; Vanneste & Yavneh 2007; Gula *et al.* 2009).

Funding from the French National Agency for Research (ANR) under grant no. BLAN06-3-137005 (Flowing Project) is gratefully acknowledged.

#### REFERENCES

- BALMFORTH, N. J. 1999 Shear instability in shallow water. *J. Fluid Mech.* **387**, 97–127.
- BILLANT, P. & CHOMAZ, J.-M. 2000 Experimental evidence for a new instability of a vertical columnar vortex pair in a strongly stratified fluid. *J. Fluid Mech.* **418**, 167–188.
- BILLANT, P. & GALLAIRE, F. 2005 Generalized Rayleigh criterion for non-axisymmetric centrifugal instabilities. *J. Fluid Mech.* **542**, 365–379.
- BILLANT, P. & LE DIZÈS, S. 2009 Waves on a columnar vortex in a strongly stratified fluid. *Phys. Fluids*. **21**, 106602.
- BOUBNOV, B. M., GLEDZER, E. B. & HOPFINGER, E. J. 1995 Stratified circular Couette flow: instability and flow regimes. *J. Fluid Mech.* **292**, 333–358.
- BOULANGER, N., MEUNIER, P. & LE DIZÈS, S. 2007 Structure of a tilted stratified vortex. *J. Fluid Mech.* **583**, 443–458.
- BOULANGER, N., MEUNIER, P. & LE DIZÈS, S. 2008 Instability of a tilted vortex in stratified fluid. *J. Fluid Mech.* **596**, 1–20.
- BRIGGS, R. J., DAUGHERTY, J. D. & LEVY, R. H. 1970 Role of Landau damping in cross-field electron beams and inviscid shear flow. *Phys. Fluids* **13** (6), 421–432.
- BROADBENT, E. G. & MOORE, D. W. 1979 Acoustic destabilization of vortices. *Phil. Trans. R. Soc. A* **290**, 353–371.
- CAIRNS, R. A. 1979 The role of negative energy waves in some instabilities of parallel flows. *J. Fluid Mech.* **92**, 1–14.
- ELOY, C. & LE DIZÈS, S. 1999 Three-dimensional instability of Burgers and Lamb–Oseen vortices in a strain field. *J. Fluid Mech.* **378**, 145–166.
- ESCH, R. E. 1957 The instability of a shear layer between two parallel streams. *J. Fluid Mech.* **3**, 289–303.
- FABRE, D. & JACQUIN, L. 2004 Viscous instabilities in trailing vortices at large swirl numbers. *J. Fluid Mech.* **500**, 239–262.
- FABRE, D., SIPP, D. & JACQUIN, L. 2006 The Kelvin waves and the singular modes of the Lamb–Oseen vortex. *J. Fluid Mech.* **551**, 235–274.

- FORD, R. 1994 The instability of an axisymmetric vortex with monotonic potential vorticity in rotating shallow water. *J. Fluid Mech.* **280**, 303–334.
- FUKUMOTO, Y. 2003 The three-dimensional instability of a strained vortex tube revisited. *J. Fluid Mech.* **493**, 287–318.
- GULA, J., PLOUGONVEN, R. & ZEITLIN, V. 2009 Ageostrophic instabilities of fronts in a channel in a stratified rotating fluid. *J. Fluid Mech.* **627**, 485–507.
- HALL, I. M., BASSOM, A. P. & GILBERT, A. D. 2003 The effect of viscosity on the stability of planar vortices with fine structure. *Quart. J. Mech. Appl. Math.* **56**, 649–657.
- HAYASHI, Y.-Y. & YOUNG, W. R. 1987 Stable and unstable shear modes of rotating parallel flows in shallow waters. *J. Fluid Mech.* **184**, 477–504.
- HEALEY, J. J. 2006 A new convective instability of the rotating-disk boundary layer with growth normal to the disk. *J. Fluid Mech.* **560**, 279–310.
- HODYSS, D. & NOLAN, D. S. 2008 The Rossby-inertia-buoyancy instability in baroclinic vortices. *Phys. Fluids* **20**, 096602.
- KELVIN, LORD 1880 Vibrations of a columnar vortex. *Phil. Mag.* **10**, 155–168.
- KNESSL, C. & KELLER, J. B. 1992 Stability of rotating shear flows in shallow water. *J. Fluid Mech.* **244**, 605–614.
- LE BARS, M. & LE GAL, P. 2007 Experimental analysis of the stratorotational instability in a cylindrical Couette flow. *Phys. Rev. Lett.* **99**, 064502.
- LE DIZÈS, S. 2000 Non-axisymmetric vortices in two-dimensional flows. *J. Fluid Mech.* **406**, 175–198.
- LE DIZÈS, S. 2004 Viscous critical-layer analysis of vortex normal modes. *Stud. Appl. Math.* **112** (4), 315–332.
- LE DIZÈS, S. 2008 Inviscid waves on a Lamb–Oseen vortex in a rotating stratified fluid: consequences on the elliptic instability. *J. Fluid Mech.* **597**, 283–303.
- LE DIZÈS, S. & BILLANT, P. 2006 Instability of an axisymmetric vortex in a stably stratified fluid. In *Sixth European Fluid Mechanics Conference*, Stockholm, Sweden.
- LE DIZÈS, S. & BILLANT, P. 2009 Radiative instability in stratified vortices. *Phys. Fluids* **21**, 096602.
- LE DIZÈS, S. & LACAZE, L. 2005 An asymptotic description of vortex Kelvin modes. *J. Fluid Mech.* **542**, 69–96.
- LE DIZÈS, S. & LAPORTE, F. 2002 Theoretical predictions for the elliptic instability in a two-vortex flow. *J. Fluid Mech.* **471**, 169–201.
- LESSEN, M. & PAILLET, F. 1974 The stability of a trailing line vortex. Part 2. Viscous theory. *J. Fluid Mech.* **65**, 769–779.
- LUO, K. H. & SANDHAM, N. D. 1997 Instability of vortical and acoustic modes in supersonic round jets. *Phys. Fluids* **9**, 1003–13.
- MEUNIER, P. & LEWEKE, T. 2005 Elliptic instability of a co-rotating vortex pair. *J. Fluid Mech.* **533**, 125–159.
- MIYAZAKI, T. & FUKUMOTO, Y. 1991 Axisymmetric waves on a vertical vortex in a stratified fluid. *Phys. Fluids A* **3**, 606–616.
- MOLEMAKER, M. J., MCWILLIAMS, J. C. & YAVNEH, I. 2001 Instability and equilibration of centrifugally stable stratified Taylor–Couette flow. *Phys. Rev. Lett.* **86**, 5270–5273.
- MOLEMAKER, M. J., MCWILLIAMS, J. C. & YAVNEH, I. 2005 Baroclinic instability and loss of balance. *J. Phys. Oceanogr.* **35**, 1505–1517.
- NARAYAN, R., GOLDREICH, P. & GOODMAN, J. 1987 Physics of modes in a differentially rotating system – analysis of the shearing sheet. *Mon. Not. R. Astron. Soc.* **228**, 1–41.
- OTHEGUY, P., CHOMAZ, J.-M. & BILLANT, P. 2006 Elliptic and zigzag instabilities on co-rotating vertical vortices in a stratified fluid. *J. Fluid Mech.* **553**, 253–272.
- PAPALOIZOU, J. C. B. & PRINGLE, J. E. 1984 The dynamical stability of differentially rotating disks with constant specific angular momentum. *Mon. Not. R. Astron. Soc.* **208**, 721–750.
- SAKAI, S. 1989 Rossby–Kelvin instability: a new type of ageostrophic instability caused by a resonance between Rossby waves and gravity waves. *J. Fluid Mech.* **202**, 149–176.
- SATOMURA, T. 1981 An investigation of shear instability in a shallow water. *J. Meteorol. Soc. Jpn* **59**, 148–167.
- SCHecter, D. A. 2008 The spontaneous imbalance of an atmospheric vortex at high Rossby number. *J. Atmos. Sci.* **65**, 2498–2521.

- SCHECTER, D. A., DUBIN, D. H. E., CASS, A. C., DRISCOLL, C. F., LANSKY, I. M. & O'NEIL, T. M. 2000 Inviscid damping of asymmetries on a two-dimensional vortex. *Phys. Fluids* **12** (10), 2397–2412.
- SCHECTER, D. A. & MONTGOMERY, M. T. 2004 Damping and pumping of a vortex Rossby wave in a monotonic cyclone: critical layer stirring versus inertia–buoyancy wave emission. *Phys. Fluids* **16**, 1334–48.
- SCHECTER, D. A. & MONTGOMERY, M. T. 2006 Conditions that inhibit the spontaneous radiation of spiral inertia–gravity waves from an intense mesoscale cyclone. *J. Atmos. Sci.* **63**, 435–456.
- SCHECTER, D. A., MONTGOMERY, M. T. & REASOR, P. D. 2002 A theory for the vertical alignment of a quasigeostrophic vortex. *J. Atmos. Sci.* **59** (2), 150–168.
- VANNESTE, J. & YAVNEH, I. 2007 Unbalanced instabilities of rapidly rotating stratified shear flows. *J. Fluid Mech.* **584**, 373–396.
- WILLIAMS, P. D., HAINE, T. W. N. & READ, P. L. 2005 On the generation mechanisms of short-scale unbalanced modes in rotating two-layer flows with vertical shear. *J. Fluid Mech.* **528**, 1–22.
- WITHJACK, E. M. & CHEN, C. F. 1974 An experimental study of Couette instability of stratified fluids. *J. Fluid Mech.* **66**, 725–737.
- WITHJACK, E. M. & CHEN, C. F. 1975 Stability analysis of rotational Couette flow of stratified fluids. *J. Fluid Mech.* **68**, 157–175.
- YAVNEH, I., MCWILLIAMS, J. C. & MOLEMAKER, M. J. 2001 Non-axisymmetric instability of centrifugally stable stratified Taylor–Couette flow. *J. Fluid Mech.* **448**, 1–21.